Journal of Structural Chemistry. Vol. 59, No. 7, pp. 1518-1533, 2018.

MOLECULAR ADDUCTS OF ISONIAZID: CRYSTAL STRUCTURE, ELECTRONIC PROPERTIES, AND HIRSHFELD SURFACE ANALYSIS

A. S. Kamalakaran

Three molecular adducts of the antituberculosis drug isoniazid (INH) are synthesized with γ-resorcylic acid (γRA), phloroglucinol (PG), and gallic acid (GA). The new solid phases are preliminarily characterized by the thermal analysis (DSC/TGA) and powder X-ray diffraction. The formation of new solid phases is confirmed by single crystal X-ray diffraction, infrared (FT-IR) and Raman spectroscopy. All three new solid crystalline forms are stabilized by various hydrogen bonding interactions such as $N^{+}\cdots H–O^{-}$, N···H–O, O···H–O, and π–π stacking. The FT-IR analysis puts forward that the solid form of **INH1** is a salt whereas the **INH2** and **INH3** molecular complexes are cocrystals. We have also investigated the density of states (DOS), band structure, and atomic orbit projected density of state (PDOS) of title compounds by adopting the density functional theory (DFT) technique in the local density approximation (LDA). The electronic structure calculations show that energy states are delocalized in the *k*-space due the hydrogen and covalent bonds in the crystals. The frontier molecular orbital (FMO) analysis reveals that charge transfer takes place within the compounds. The Hirshfeld analysis shows that H–H and N···H–O hydrogen bonding interactions are dominant in all three molecular adducts of INH.

DOI: 10.1134/S002247661807003X

Keywords: isoniazid, cocrystals, molecular salts, X-ray diffraction studies, Hirshfeld analysis.

INTRODUCTION

Cocrystals are multicomponent crystalline solid forms in which individual neutral molecules are bound together by non-covalent interactions, mainly hydrogen bonding patterns [1-5]. Cocrystallization and salt formation are widely used techniques in the pharmaceutical industry to address the physicochemical issues such as solubility, bioavailability, and stability of active pharmaceutical ingredients (APIs) [6-8]. The advantages of cocrystals and salts alter the physicochemical properties without compromising the intended bioactivity of an API and also give rise to the possibility of combing two or more drugs for the synergistic effect [9]. Salts differ from the cocrystals by proton transfer from the acidic functionality to the basic moiety, whereas no such proton transfer occurs in cocrystals [10, 11]. For the appropriate formation of a cocrystal or salt, the suitable coformer can be selected from the Generally Regarded as Safe (GRAS) list approved by US FDA, the pharmaceutically acceptable salts formers list [12], and the Everything Added to Food in the United States (EAFUS) list.

Department of Chemistry, School of Engineering, Dayananda Sagar University, Kudlu Gate, Bangalore, India; anands-chem@dsu.edu.in. The text was submitted by the authors in English. *Zhurnal Strukturnoi Khimii*, Vol. 59, No. 7, pp. 1580-1595, September-October, 2018. Original article submitted August 17, 2017.

Apart from the possible coformers from these lists, formulation excipients [13] and nutraceuticals are also used in the formation of cocrystals.

INH is a widely used drug alone in the prophylaxis and in combination with other antituberculosis drugs in the treatment of all forms of tuberculosis [14]. In recent years INH has drawn much attention from the crystal engineering community due to its robust interactions with molecules having carboxylic acid groups to obtain pharmaceutical cocrystals [15]. INH is a versatile cocrystal due to its pyridine and hydrazide functional groups, which results in the formation of binary crystalline phases and robust supramolecular architectures. Carboxylic acid-pyridine heterosynthons containing INH cocrystals with 4-aminosalicylic acid [16], *p*-coumaric acid [17], hydroxybenzoic and dicarboxylic acids [18-20] have been reported. In addition to carboxylic acid-pyridine heterosynthons, hydrazide-hydrazide homosynthons also form in the crystal structures of INH cocrystals with 2,2′-dithiobenzoic acid [21]. Polymorphic INH cocrystals with suberic and cinnamic acids were also reported [22]. The structure and electronic properties of boron nitride nanotubes with INH have been reported [23]. So far, there has been no study on the electronic properties of title compounds. Due to the important role of the hydrogen bond in determining the structures and peculiarity of the INH cocrystals, in this article, we discuss the effect of its electronic characteristic by studying the density of state (DOS), band structure (BS), and atomic orbit projected density of state (PDOS). PDOS is one of the important tools to understand the bond nature [24]. In this paper one molecular salt and two cocrystals of INH are reported. The primary objective of the study was to investigate the electronic properties of the title compounds and the investigation of hydrogen bonding interactions in the crystal structures of the title compounds. Three molecular salts were synthesized and studied in the present work. The chemical structures of the compounds used in this study are shown in Scheme 1.

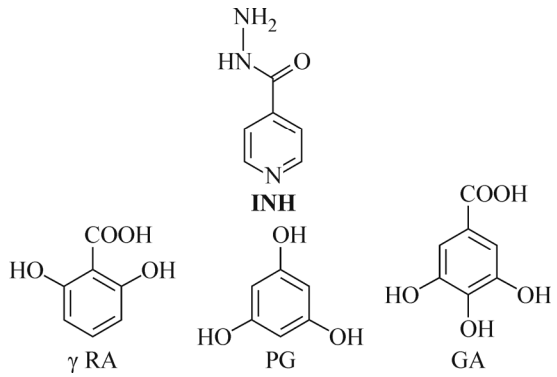

Scheme 1. Molecular structures of INH, γRA, PG and GA.

MATERIALS AND METHODS

Materials. INH, γRA, PG, and GA were purchased from Sigma-Aldrich and used as received. Solvents with HPLC grade purity were purchased from Rankem Chemicals (India) and used without further purification.

Preparation of cocrystals. Isoniazid, (γ-resorcylic acid)$_2$ salt, INH1. The 1:1 stoichiometric ratio of INH (50 mg, 0.36 mmol) and γ-resorcylic acid (55 mg, 0.36 mmol) were added into a conical flask and dissolved in methanol (3 ml) at 60 °C for 10 min. The resulting solution was filtered and left for slow evaporation at room temperature. Yellow thin rectangular crystals were obtained after two days.

(Isoniazid)$_2$. (Phloroglucinol) co-crystal, INH2. The 1:1 stoichiometric ratio of INH (50 mg, 0.36 mmol) and phloroglucinol (46 mg, 0.36 mmol) were added into a conical flask and dissolved in methanol (3 ml) at 60 °C for 10 min. The resulting solution was filtered and left for slow evaporation at room temperature. Brown diamond shape crystals were obtained after seven days.

(Isoniazid). (Gallic acid) co-crystal, INH3. The 1:1 stoichiometric ratio of INH (50 mg, 0.36 mmol) and gallic acid (62 mg, 0.36 mmol) were added into a conical flask and dissolved in methanol (3 ml) at 60 °C for 10 min. The resulting solution was filtered and left for slow evaporation at room temperature. Brown small rectangular block type crystals were obtained after four days.

Single crystal X-ray diffraction measurements for all three multicomponent solid forms were carried out on a Bruker AXS Kappa Apex2 CCD diffractometer with MoK_α radiation at 293 K [25]. Data reduction was performed with the SAINT program [25] and the structure was solved using the SIR92 program [26]. The SHELXL97 program was used for the structure refinement [27]. Structure-invariant direct methods were used for primary atom site locations and secondary atom site locations were found from the difference Fourier map. Hydrogen atom site locations were inferred from the neighbouring sites. Table 1 summarizes the crystallographic data on **INH1**, **INH2**, and **INH3**.

Powder X-ray diffraction (PXRD) data for all compounds were collected at 293 K on a Bruker D8 Advance diffractometer which employs a sealed tube Cu X-ray source (λ = 1.5406 Å), operating at 30 kV and 10 mA, and a LynxEye PSD detector in the Bragg-Brentano geometry.

Differential scanning calorimetry (DSC) data were collected on a DSC 200 F3, Netzsch, Germany calorimeter. Experimental conditions employed: 40 µl aluminium crucibles sealed with lids, dry nitrogen atmosphere with a 50 ml/min^1 flow rate, a heating rate of 10 °C/min^1 in the heating range from 30 °C to 250 °C.

Thermal gravimetric analysis (TGA) data were collected on TGA Q5000 V3. 10 Build 258. Experimental conditions: 70 ml alumina crucibles, dry nitrogen atmosphere with a 50 ml/min^1 flow rate, a heating rate of 5 °C/min^1.

TABLE 1. Crystallographic Summary for **INH1**, **INH2** and **INH3**

Parameter	**INH1**	**INH2**	**INH3**
Formula	$C_{20}H_{19}N_3O_9$	$C_{18}H_{20}N_6O_5$	$C_{13}H_{13}N_3O_6$
Molecular weight	445.38	400.40	307.26
Crystal system	Triclinic	Monoclinic	Triclinic
Space group	*P*-1	$P2_1/c$	*P*-1
a, Å	7.6120(1)	7.2700(1)	8.7080(2)
b, Å	7.8310(1)	9.1710(1)	11.9200(2)
c, Å	17.8330(3)	27.8830(5)	13.3900(2)
α, deg.	81.883(1)	90	93.711(1)
β, deg.	88.737(1)	93.744(1)	98.735(1)
γ, deg.	64.744(1)	90	108.199(1)
Volume, Å^3	950.91(3)	1855.08(5)	1295.69(4)
Z	2	4	4
D_x, g/cm^3	1.556	1.434	1.575
F(000)	464.0	840.0	640.0
μ(MoK_α), mm^{-1}	0.125	0.108	0.127
Crystal size, mm	0.30×0.30×0.20	0.35×0.30×0.30	0.30×0.20×0.20
Temperature, K	293	293	293
θ range for data collection, deg.	2.3-31.8	2.3-32.4	2.5-30.1
R_1 / wR_2	0.0360 / 0.1061	0.0360 / 0.0992	0.0522 / 0.1730
Goodness-of-fit	1.028	1.051	1.091
Parameters	298	286	453
Reflections collected	16189	16460	21271
Unique reflections	3336	3265	4522
Observed reflections	2978	2713	3247
CCDC No.	906097	912495	917543

Infrared spectroscopy (FTIR). A Bruker Alpha-T FT-IR spectrophotometer in the spectral range from 4000 cm^{-1} to 400 cm^{-1} with a resolution of 2 cm^{-1} was used to record the IR spectra of the starting materials and molecular salts (1a) and (1b). The KBr pellet method was employed to record the IR spectra.

Raman spectroscopy (FT Raman). FT-Raman spectra of all three compounds were recorded on a Bruker RFS 27, stand-alone Fourier transform Raman spectrometer, using the KBr pellet method in the spectral range 4000 cm^{-1} to 50 cm^{-1} with resolution of 2 cm^{-1}.

COMPUTATIONAL DETAILS

The input data for theoretical calculations was taken from the crystal structural data of one salt and two INH cocrystals. Then the optimization (relaxation) of the unit cell parameters and the atomic coordinates in the crystals were performed using the Broyden-Fcetcher-Goldfarb-Shanne (BFGS) algorithm, as implemented in the CASTEP code [28, 29]. The self-consistent convergence accuracy was set at 2×10^{-5} eV/atom. The convergence and criterion of the largest force on atoms was 0.05 eV/Å, the stress was no more than 0.1 GPa, and the maximum displacement was 2×10^{-4} nm. The band structure along with the density of states (DOS) were calculated on the corresponding optimized crystal geometries with density functional theory (DFT) using the local density approximation (LDA) with the CA-PZ functional implemented in the CASTEP code, which uses a plane wave basis set for the valence electrons and the ultrasoft pseudopotential for the core electrons. The number of plane waves included in the basis set was determined by a cut-off energy E_c of 300 eV, and the numerical integration of the Brillouin zone was performed using a 2×2×1 Monkhorst-Pack *k*-point sampling. Pseudoatomic calculations were performed for H $1s^1$, C $2s^2 2p^2$, N $2s^2 2p^3$, and O $2s^2 2p^4$. All the calculation was carried out in the reciprocal space.

The structure of the INH cocrystals undergoing restricted thermal motion in a crystal field and measured by single crystal X-ray diffraction was discussed in the previous section. The structure of the isolated cocrystals is the definitive structure from the point of view of a theoretical chemist. The initial conformations for using in the DFT calculations were taken from the experimental structural data obtained from X-ray crystallography. The ground-state energies and optimized geometries were calculated for monomers of the title compounds in the gas phase using DFT. The DFT calculations were performed using the Gaussian 09 Rev A.2 program [30]. All calculations were made at the B3LYP/6-31G(*d*,*p*) level. The optimized geometries of three monomers were very close to the conformation in the crystal structures, indicating that monomers are in a relaxed conformation. The calculated optimised bond lengths and bond angles of the crystal and monomer structures of the title compounds were compared with the experimental data and are presented in Table 2.

Molecular Hirshfeld surfaces were generated by the CrystalExplorer [31] computer program. The Hirshfeld surface is an easily interpretable visualization of a molecule within its environment. The 2D fingerprint maps obtained from the reduced Hirshfeld surfaces provide the full distribution of intermolecular interactions. The principles of Hirshfeld surfaces were reported elsewhere [32, 33]. In this work, we performed the Hirshfeld surface analysis on the present three INH cocrystals to investigate the effect of different phenolics and carboxylic acids on the intermolecular interactions of the INH molecule.

DISCUSSION

Single crystal XRD analysis. (Isoniazid). (γ-Resorcylic acid)$_2$ salt, INH1. The structural determination shows that **INH1** forms a 1:2 molecular salt in the triclinic $P\bar{1}$ space group with $Z = 2$. The asymmetric unit of **INH1** consists of one diprotonated INH and two γ-resorcylate anions in the asymmetric unit (Fig. 1). The pyridine nitrogen atom (N1) and the terminal nitrogen atom (N3) of the carbohydrazide fragment in INH are completely protonated by the carboxylic acid group of two γRA molecules where the –OH groups remained unionized. The carboxylate group on γRA is involved in the intramolecular hydrogen bonding with both phenolic groups (Fig. 2). The aromatic molecular core of the γRA molecule is π-stacked infinitely along the crystallographic *a* axis at a 3.77 Å distance.

TABLE 2. Selected Bond Lengths (Å) and Bond Angles (deg.) for **INH1**, **INH2** and **INH3**

Com-pound	Parameters	Calculated B3LYP/6-31G(*d*,*p*)	Experimental X-Ray	Parameters	Calculated B3LYP/6-31G(*d*,*p*)	Experimental X-Ray
INH1		Bond lengths			Bond Angles	
	C(1)–O(2)	1.282	1.262(18)	O(2)–C(1)–O(1)	121.327	122.30(14)
	C(1)–O(1)	1.288	1.265(18)	C(18)–N(1)–C(19)	122.350	121.76(15)
	C(3)–O(3)	1.345	1.354(19)	O(5)–C(8)–O(6)	122.350	122.70(16)
	C(7)–O(4)	1.339	1.352(19)			
	C(8)–O(5)	1.272	1.246(2)			
	C(8)–O(6)	1.291	1.277(2)			
	C(18)–N(1)	1.338	1.328(2)			
	C(19)–N(1)	1.339	1.332(2)			
	C(15)–O(9)	1.237	1.212(19)			
INH2		Bond lengths			Bond Angles	
	C(1)–O(1)	1.349	1.363(8)	C(10)–N(1)–C(11)	118.447	116.4(6)
	C(3)–O(2)	1.344	1.358(8)	N(6)–N(5)–H(5A)	115.651	115(5)
	C(5)–O(3)	1.342	1.360(8)	N(5)–N(6)–H(6B)	109.765	107(6)
	C(11)–N(1)	1.337	1.328(10)	N(5)–N(6)–H(6A)	108.233	106(6)
	C(17)–N(4)	1.333	1.326(10)			
	N(2)–N(3)	1.405	1.418(8)			
	N(5)–N(6)	1.402	1.413(8)			
INH3		Bond lengths			Bond Angles	
	C(13)–O(3)	1.271	1.213(3)	C(1)–N(1)–C(5)	121.111	117.8(2)
	C(20)–O(9)	1.248	1.213(3)	C(10)–N(4)–C(9)	120.264	117.3(2)
	N(2)–N(3)	1.404	1.415(3)	N(3)–N(2)–H(2A)	112.446	111(2)
	N(5)–N(6)	1.395	1.413(3)	N(2)–N(3)–H(3A)	109.112	104(3)
	C(6)–O(1)	1.246	1.217(3)			
	C(12)–O(2)	1.255	1.223(3)			

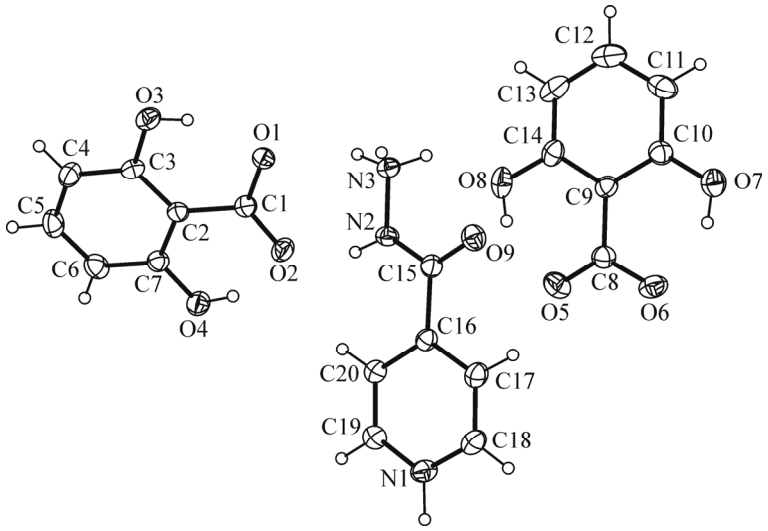

Fig. 1. The contents of asymmetric unit of **INH1**, showing the atom numbering scheme. Displacements of ellipsoids are drawn at 50% probability level.

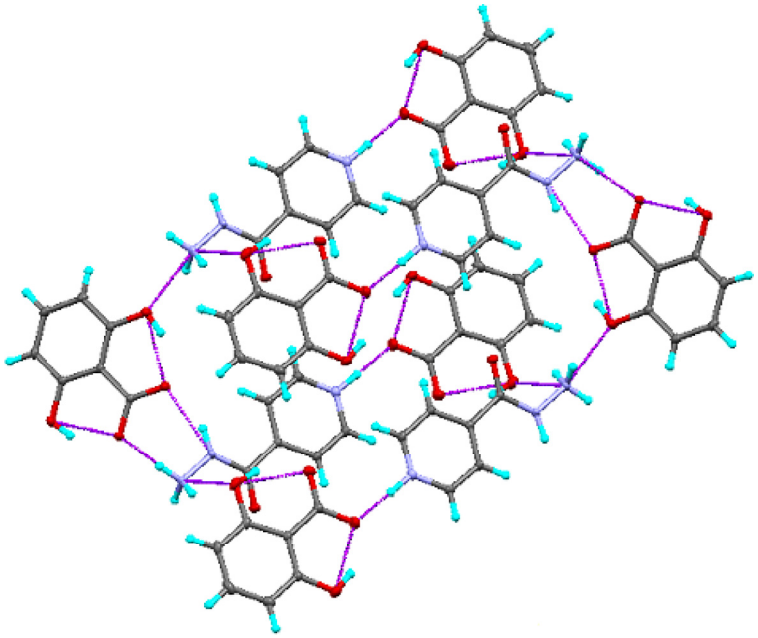

Fig. 2. Perspective view of the supramolecular assembly of **INH1**.

(Isoniazid)$_2$. (Phloroglucinol) co-crystal, INH2. The crystal structure of **INH2** consists of two isoniazid molecules and one phloroglucinol molecule in the asymmetric unit (Fig. 3) and is crystallized in the monoclinic $P2_1/c$ space group with $Z = 4$. The **INH2** crystal structure has been stabilized by two phenolic OH···$N_{pyridine}$*D* heterosynthons and one phenolic OH···$N_{1\ amine}$*D* heterosynthon. The **INH2** cocrystal also has 1° amine···carbonyl R_2^2 (10) homosynthon, 1°amine···2°amine R_2^2 (6) homosynthon, and 2° amine···carbonyl *D* heterosynthon. In **INH2** the carbohydrazide moiety of INH is linked to a similar group in another molecule in a head-to-head arrangement, forming a carbohydrazide···carbohydrazide homosynthon, which resembles amide dimers in primary amides and this homosynthon is not found in the crystal packing of INH itself. The terminal nitrogen atom of the hydrazide moiety accepts an N···H–O hydrogen bonding from the phenolic group of phloroglucinol. The pyridine nitrogen atom also accepts an N···H–O hydrogen bonding from the phenolic group of phloroglucinol which produces the phenol···pyridine heterosynthon. The hydrogen atom of the secondary amine of the

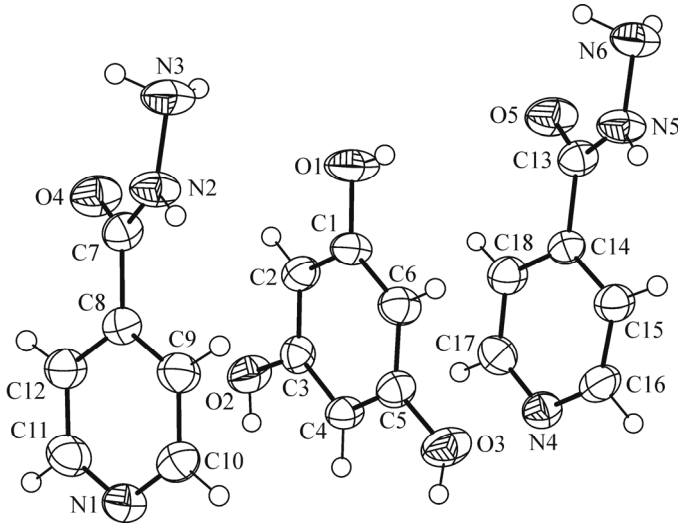

Fig. 3. The contents of asymmetric unit of **INH2**, showing the atom numbering scheme. Displacements of ellipsoids are drawn at 50% probability level.

TABLE 3. Hydrogen Bonding Geometrical Parameters of **INH1**, **INH2** and **INH3**

D–H···A	*d*(D–H), Å	*d*(H···A), Å	*d*(D···A), Å	∠(D–H···A), deg.	Symmetry transformations
INH1					
N(3)–H(3A)···O(1)	0.89	1.98	2.6540(17)	131.4	
N(3)–H(3B)···O(8)	0.89	2.16	2.9117(19)	141.8	
N(3)–H(3C)···O(3)	0.89	2.03	2.881(2)	160.1	–*x*+3, –*y*, –*z*
O(3)–H(3)···O(1)	0.82	1.81	2.5364(16)	147.6	
O(4)–H(4A)···O(2)	0.82	1.79	2.5255(15)	148.0	
O(7)–H(7)···O(6)	0.82	1.78	2.5103(18)	147.7	
O(8)–H(8)···O(5)	0.82	1.79	2.5232(19)	148.4	
N(2)–H(2A)···O(2)	0.906(15)	1.823(16)	2.6788(17)	156.7(19)	
N(1)–H(1A)···O(6)	0.957(16)	1.617(17)	2.5729(19)	177(2)	–*x*+3, –*y*, –*z*+1
INH2					
O(1)–H(1)···N(6)	0.82	1.97	2.783(8)	172.8	–*x*+1, –*y*, –*z*+2
O(2)–H(2B)···N(4)	0.82	1.93	2.743(8)	168.8	–*x*+1, *y*+1/2, –*z*+3/2
O(3)–H(3)···N(1)	0.82	1.99	2.804(8)	169.4	–*x*, *y*–1/2, –*z*+3/2
N(5)–H(5A)···O(4)	0.88(6)	2.09(6)	2.944(7)	164(7)	*x*, *y*–1, *z*
N(2)–H(2A)···N(3)	0.89(9)	2.23(8)	3.007(9)	147(7)	–*x*, –*y*+1, –*z*+2
N(3)–H(3B)···O(1)	0.90(6)	2.33(8)	3.080(9)	140(7)	–*x*+1, –*y*+1, –*z*+2
N(3)–H(3A)···O(5)	0.89(7)	2.23(7)	3.101(10)	169(9)	–*x*+1, –*y*+1, –*z*+2
N(6)–H(6B)···O(5)	0.94(7)	2.17(9)	2.935(8)	137(7)	–*x*+2, –*y*, –*z*+2
N(6)–H(6A)···O(4)	0.95(7)	2.20(7)	3.126(9)	168(8)	–*x*+1, –*y*+1, –*z*+2
INH3					
O(6)–H(7)···N(3)	0.84(4)	1.89(4)	2.715(3)	170(4)	*x*–1, *y*, *z*
O(11)–H(12A)···N(6)	0.89(4)	1.83(4)	2.699(3)	168(4)	*x*+1, *y*, *z*–1
O(4)–H(4A)···N(1)	0.93(4)	1.72(4)	2.643(3)	178(3)	*x*, *y*, *z*–1
O(7)–H(8A)···O(11)	0.78(3)	2.13(3)	2.823(2)	148(3)	
O(10)–H(11A)···O(1)	0.88(4)	1.83(4)	2.707(3)	174(3)	*x*–1, *y*–1, *z*
O(8)–H(9A)···N(4)	0.97(4)	1.70(4)	2.670(3)	177(3)	
O(5)–H(5A)···O(2)	0.87(4)	1.86(4)	2.718(3)	168(4)	*x*+1, *y*+1, *z*–1
O(12)–H(13A)···O(6)	0.86(4)	2.06(4)	2.781(2)	141(4)	
N(2)–H(2A)···O(12)	0.90(4)	2.14(4)	2.933(3)	146(3)	*x*+1, *y*, *z*
N(5)–H(5B)···O(7)	0.84(3)	2.21(3)	2.952(3)	147(3)	*x*–1, *y*, *z*+1
N(3)–H(3B)···O(3)	0.90(4)	2.25(4)	3.112(4)	160(3)	–*x*+2, –*y*+2, –*z*
N(6)–H(6B)···O(4)	0.85(3)	2.66(3)	3.501(4)	170(3)	–*x*, –*y*+1, –*z*+1
N(3)–H(3A)···O(2)	0.98(5)	2.51(4)	3.255(4)	133(3)	–*x*, –*y*+1, –*z*+1

carbohydrazide fragment participates in the hydrogen bonding with the carbonyl group of the carbohydrazide moiety in another INH molecule. The hydrazine moiety (–NH–NH_2) of INH is linked to a similar group in another molecule forming a hydrazine···hydrazine homosynthon which is also not present in the crystal packing of INH itself (Fig. 4).

(Isoniazid). (Gallic acid) co-crystal, INH3. The crystal structure of **INH3** has one INH and one gallic acid molecules in the asymmetric unit (Fig. 5) and is crystallized in the triclinic $P\bar{1}$ space group with $Z = 4$. In **INH3** the carboxylic acid···pyridine hydrogen bonding heterosynthon *D* is supported by the C–H···O hydrogen bond, forming an expected $R_2^2(7)$ heterosynthon. The two phenolic –OH groups in gallic acid are linked to the similar phenolic –OH groups in another

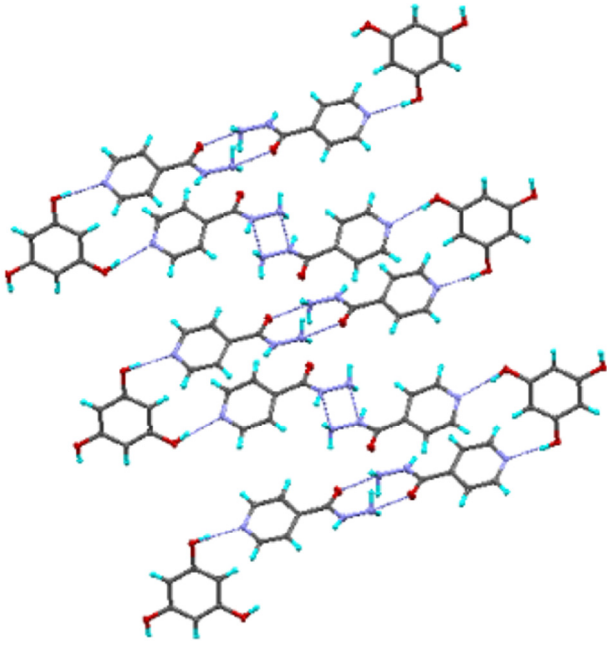

Fig. 4. 1D chain motif of **INH2**.

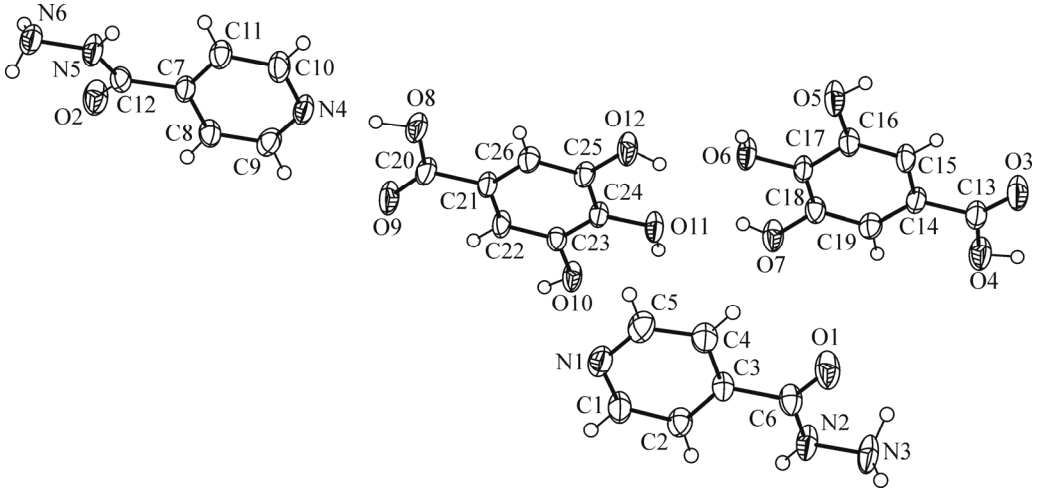

Fig. 5. The contents of asymmetric unit of **INH3**, showing the atom numbering scheme. Displacements of ellipsoids are drawn at 50% probability level.

molecule forming the $R_2^2(10)$ homosynthon. A new heterosynthon $R_3^3(7)$ is formed by the interaction of two phenolic –OH groups of gallic acid with the hydrazine moiety of INH (Fig. 6).

FT-IR and FT-Raman spectroscopy. FT-IR spectroscopy is a very useful technique to characterize and distinguish cocrystals from salts [34, 35]. INH shows an IR absorption frequency for an amide C=O stretching at 1667 cm^{-1}, primary amine N–H stretching at 3304 cm^{-1} and 3112 cm^{-1}. However, changes were observed in the IR peaks of API as well as the coformers in all three multicomponent solid forms. The carboxylic acid C=O IR absorption frequency of γ-resorcylic acid was observed at 1685 cm^{-1} which was absent in **INH1**. Moreover, the appearance of two characteristic carboxylate IR absorption vibrations at 1588 cm^{-1} and 1356 cm^{-1} in **INH1** due to asymmetric and symmetric O–C–O stretchings, respectively, confirmed the proton transfer from the –COOH group in γRA [36]. The formation of the **INH1** salt was further evidenced by the appearance of an IR absorption frequency band at 1643 cm^{-1}, which can be assigned to C=N vibrations characteristic of the quaternary nitrogen atom in a heterocyclic ring [37, 38]. In **INH2** the phenolic O–H stretching shifts from 3200 cm^{-1} to 3283 cm^{-1}, indicating that neutral INH molecules form cocrystals with neutral PG molecules. The carbo-

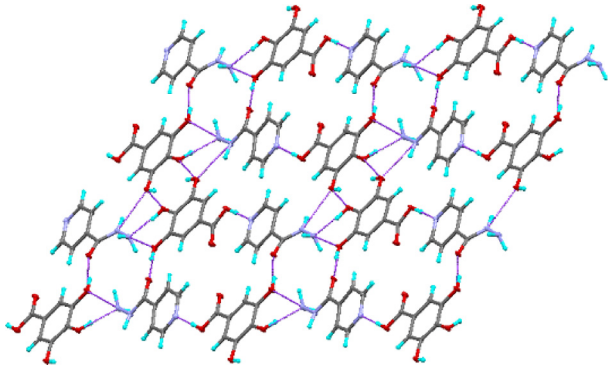

Fig. 6. Perspective view of the supramolecular layered assembly of **INH3**.

hydrazide C=O stretching in **INH3** shifts from 1667 cm^{-1} to 1674 cm^{-1} and the carboxylic acid –OH IR **INH1** solid form is a salt whereas the **INH2** and **INH3** compounds are cocrystals. Similarly, the Raman spectra of all three multicomponent solid forms also exhibited substantial changes in comparison with the starting components. A comparison of the Raman stretching frequencies are summarized in Table 4.

Thermal analysis. The DSC curves of the three solid forms of INH are given in the supplementary material. The DSC thermogram of **INH1** showed a sharp endothermic peak centered at 194.9 °C absorption frequency shifts from 3286 cm^{-1} to 3319 cm^{-1}, suggesting the cocrystal formation. Thus, the FT-IR analysis suggested that the with an onset temperature at 189.2 °C, which is higher than that for the starting materials (INH, 175.4 °C; γRA, 173.5 °C). The DSC curve of **INH2** presents a single sharp endothermic peak at 177.9 °C, corresponding to its melting point. The **INH3** compound shows a single melting endothermic peak at 224.8 °C in DSC, which lies in between the melting temperatures of the starting components (INH, 175.4 °C; GA, 250.6 °C).

PXRD analysis. PXRD is a fingerprint characterization technique for the identification of new solid phases such as cocrystals and salts [39, 40]. The PXRD patterns of all three solid forms are summarized in Fig. 7. All three multicomponent solids display a unique crystalline PXRD pattern in comparison to the starting components. PXRD of **INH1** exhibited characteristic reflections at about 2θ of 9.99°, 15.01°, 20.02°, 25.19°, 27.29°, 29.46°, 30.36°, and 35.37°. The **INH2** cocrystal exhibited characteristic reflections at about 2θ of 12.69°, 19.05°, 25.71°, 26.69°, and 38.74°, whereas for **INH3** the characteristic reflections were found at 17.33°, 23.84°, and 27.74°. This indicates the formation of new multicomponent solid forms.

Band structure (BS) and density of states (DOS). Owing to the vital role of the hydrogen bonding, BS and DOS are useful in determining the structures and peculiarities of the cocrystals. On the basis of the equilibrium crystal structure, self-consistent BS along different symmetry directions of the Brillouin zone have been calculated using 12 K points (Fig. 8). Only the bands between –4 eV and 4 eV are presented for the sake of brevity. The important characteristics in Fig. 8 are that the band lines are almost very flat and vary slowly in the BZ direction Γ–Z. The energy band gap is 1.706 eV, 2.463 eV, and 1.051 eV, which corresponds to the minimum of the conduction band (CB) and the maximum of the valence band (VB) at the C point in **INH1**, **INH2**, and Z pointing **INH3**. One can also observe from Fig. 8 that the energy states are substantially delocalized in the *k*-space due to hydrogen and covalent bonds in the crystal.

TABLE 4. FT-Raman Stretching Vibration Modes (υ, cm^{-1}) for the **INH** Solid Forms

Compound	Carbohydrazide C=O	Phenolic –OH	Phenolic C–O
INH	1646	3097	1249
INH1	1631	3077	1280
INH2	1633	3064	1214
INH3	1611	3075	1257

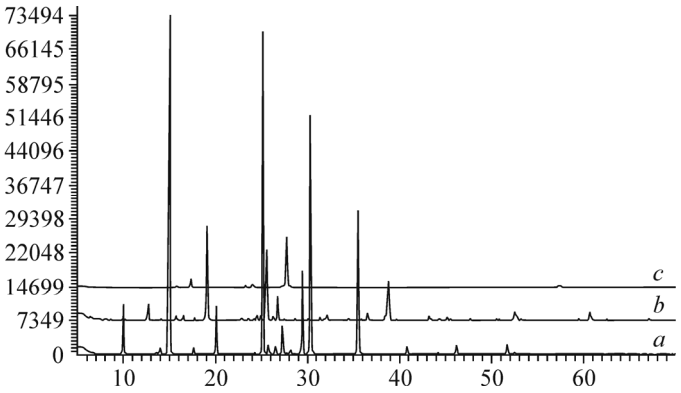

Fig. 7. PXRD patterns of the compounds **INH1** (*a*), **INH2** (*b*) and **INH3** (*c*).

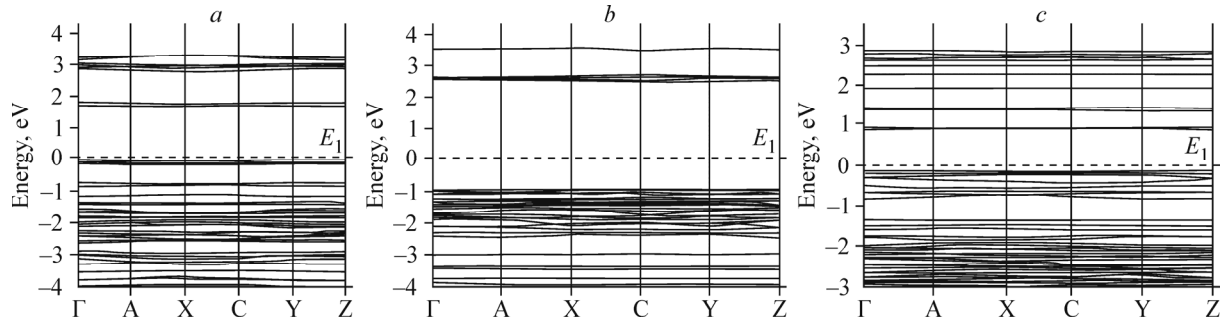

Fig. 8. The electronic band structure of **INH1** (*a*), **INH2** (*b*), **INH3** (*c*). Energy range is from –4 eV to 4 eV. The Fermi level (E_f) is indicated by a horizontal dotted line.

Many pharmaceutical cocrystals exist as two or more crystalline phases and have different conformations of the molecules in the crystal lattice. Thus, the chemical and physical properties of the cocrystals change with the crystalline phase. This is mainly due to variation in the electronic structure of the cocrystals. The variation in the electronic structure influences the processability of drug substances and the performance of drug products, such as stability, dissolution, and bioavailability. Therefore, a DOS analysis is helpful in understanding the electronic structural properties of cocrystals. A better understanding of BS is provided by partial density of state (PDOS) used to investigate the constitution of energy bands. The PDOS analysis gives a qualitative handle on the band nature, such as electron hybridization and the origin of main peaks in the optical spectra. Hence, to obtain further information about the bond nature of the one salt and two cocrystals (**INH1**, **INH2**, and **INH3**), DOS and PDOS were calculated and displayed in Fig. 9. The calculated results show that the energy band is dense around –4.54 eV, –1.32 eV, and –5.77 eV, which produces maximum DOS in **INH1**, **INH2**, and **INH3**. The Fermi energy near zero energy agrees with the band energy structure of three INH cocrystals. In the three compounds, the upper part of the valence band (N 2*p*, O 2*p*, and C 2*p* orbitals) plays the main role in the total density of states (TDOS), whereas the lower part of the conduction band is mainly formed by C 2*p* and N 2*p*; the H 1*s* and O 2*p* states also make contributions. The hybridization of atomic orbitals does not appear in the range from –5 eV to 1 eV, which is consistent with the dispersive band energy from Fig. 8. From TDOS and projected DOS for **INH1**, it is clear that O2*p* is located below E_f, implying that the O2*p* orbital is almost filled. On the other hand, projected DOS shows that the C2*p* orbital is located above the Fermi level, indicating that the orbital is almost empty. A similar situation can be observed for **INH2** and **INH3** cocrystals, respectively. To show the electronic character of the three cocrystals, we analyzed DOS and PDOS in the whole energy region in Fig. 9*b*. The O2*p* orbital is mainly located in VB, which indicates that the O atom can strongly absorb an electron and the C2*p* orbital is located almost in CB, which shows the obvious covalent character of the C atom. In addition to the covalent bond, the H and O atoms in the three compounds also tend to combine via other interactions. Consequently, we suppose the hydrogen bond to occur in salt and two cocrystals.

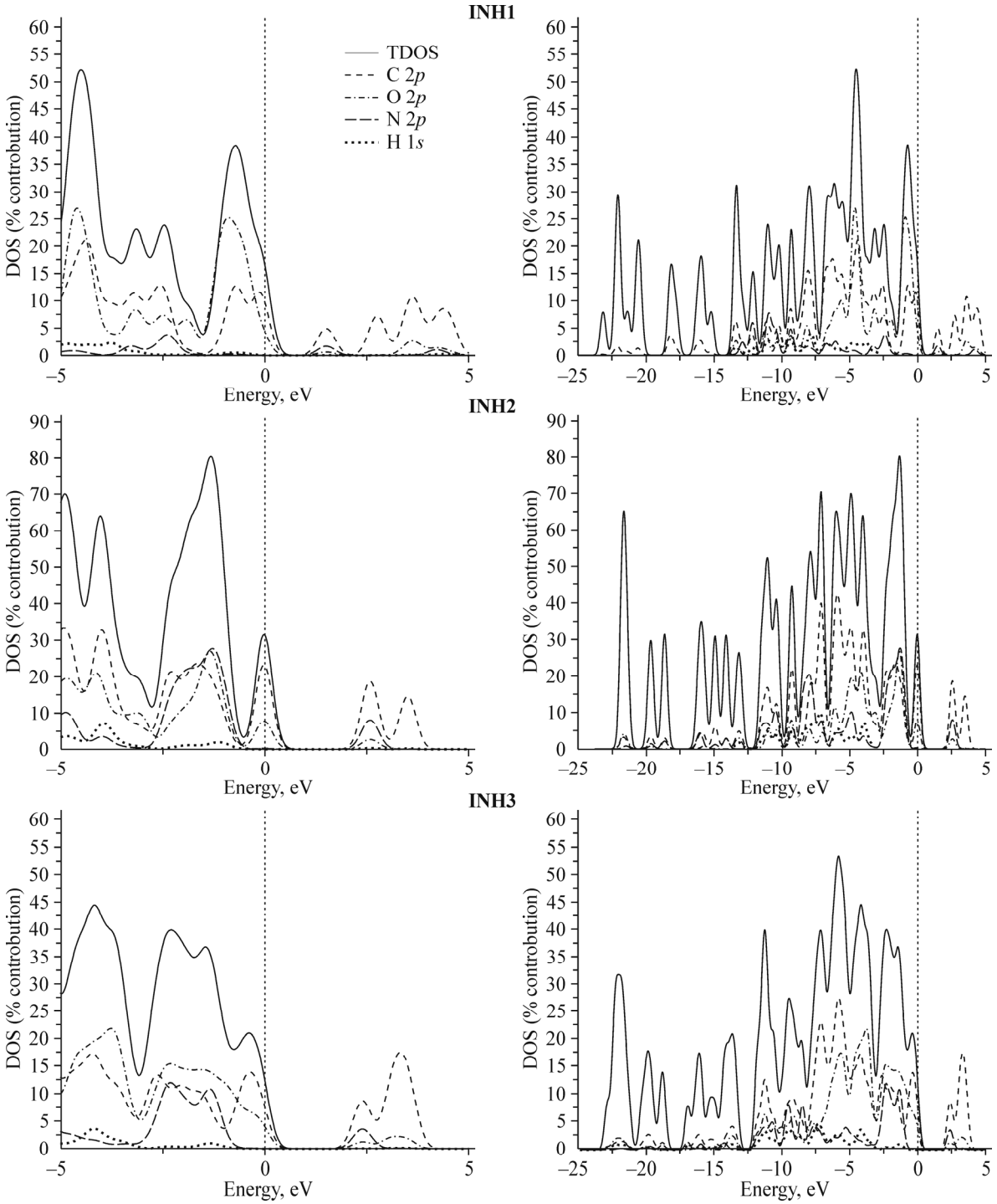

Fig. 9. Total and partial densities of states (DOS) of three co-crystals **INH1**, **INH2** and **INH3** are shown in (*a*) and (*b*). The dotted vertical lines correspond to the Fermi level. (*a*) and (*b*) shows the DOS graph of the energy range in –5 eV to 5 eV, –25 eV to 5 eV, respectively.

Energy and stability. In order to investigate the stability of the title compounds, we have calculated frontier molecular orbital (FMO) energy levels, total energy, dipole moment, and chemical hardness (η) of three isolated monomers at the B3LYP/6-31G(*d*,*p*) level, and the results were given in Table 5.

The chemical hardness is quite useful to explain the chemical stability and reactivity of chemical species. Also, the chemical hardness is useful to explain the relative stability and reactivity of chemical species. Hard species having a large

TABLE 5. Summary of the Various Contact Contributions to the **INH** Hirshfeld Surface Area in Molecular Adducts **1-3**

Compound	H–H	O–H	N–H	C–H	O–C	N–C	C–C	O–O	O–N	N–N
INH1	33.5	34.1	1.3	16.3	6.0	0.0	7.2	0.8	0.8	0.0
INH2	47.3	25.4	15.7	6.0	1.5	0.9	2.8	0.0	0.4	0.0
INH3	30.2	32.9	6.6	14.5	4.7	1.5	7.1	1.0	1.5	0.1

HOMO-LUMO gap will be more stable and less reactive than soft species having a small HOMO-LUMO gap. The hardness value of a molecule is formulated by Eq. 1 [41]

$$\eta = [-\varepsilon_{HOMO} + \varepsilon_{LUMO}]/2, \quad (1)$$

where ε_{HOMO} and ε_{LUMO} are the energies of the HOMO and LUMO orbitals. As seen from Table 5, the total energy of **INH3** is lower than those of **INH1** and **INH2**, while epy chemical hardness is in the order **INH3** > **INH2** > **INH1**, which indicates that **INH3** is more stable than **INH1** and **INH2** in the gas phase.

From the FMO energy levels of the title compounds, we can also find that the corresponding electron transfers happened between the HOMO and the LUMO. Fig. 10 shows the distributions and energy levels of FMOs computed at the B3LYP/6-31G(*d*,*p*) level for the title compounds.

As seen from Fig. 10, in the HOMO electrons are mainly delocalized on gamma resorcylic acid, phloroglucinol, and gallic acid in **INH1**, **INH2**, and **INH3** respectively. Whereas, the LUMO in three compounds, the electrons are mainly localized on the isoniazid moiety. This clearly indicates the charge transfer taking place within the title compounds.

Molecular electrostatic potential (MEP). MEP is related to the electron density and is a very useful descriptor in understanding the sites for electrophilic and nucleophilic reactions as well as the hydrogen bonding interactions [42]. To predict the reactive sites for the electrophilic and nucleophilic processes for the title compounds, the MEP surface was obtained with the B3LYP/6-31G(*d*,*p*) optimized geometry. The negative regions (left) of MEP were related to the electrophilic reactivity and the positive ones (right) to the nucleophilic reactivity (Fig. 11).

The title compounds have several possible sites for the electrophilic attack. Negative regions in the studied molecules were found around the oxygen atom. In **INH2**, a negative electrostatic potential region was also observed around the nitrogen atom. However, a maximum positive region is localized on the O–H and N–H bonds in the three compounds and indicates a possible site for the nucleophilic attack. According to these calculated results, the MEP map shows that the negative potential sites are on electronegative atoms and the positive potential sites are around the hydrogen atoms. These sites give information about the region from where the compound can have non-covalent interactions.

Hirshfeld surface analysis. The 3D Hirshfeld surfaces and 2D fingerprint plots are unique for any crystal structure as well as the polymorph. They serve as powerful tools for gaining an additional insight into the crystal structure and the polymorph comparison by color-coding short or long contacts. The 2D fingerprint plots can give a quantitative

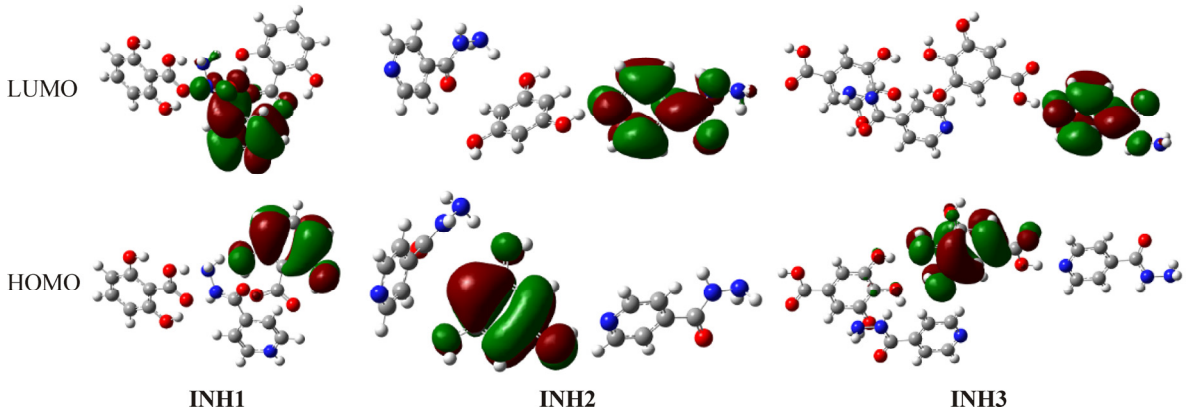

Fig. 10. HOMO and LUMO plots of three isoniazid compounds.

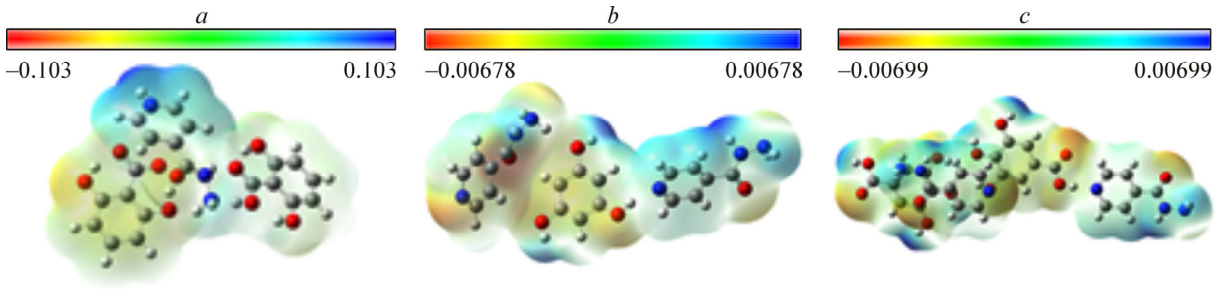

Fig. 11. Molecular electrostatic potential map (MEP) of the **INH1** (*a*), **INH2** (*b*) and **INH3** (*c*).

summarization of the nature and type of intermolecular contacts experienced by molecules in the crystal, and at the same time, it can also be broken down to give the relative contribution to the Hirshfeld surface area from each type of interactions present, quoted as the "contact contribution" [43-46]. The 3D Hirshfeld d_{norm} surfaces and 2D fingerprint maps of **INH1**, **INH2**, and **INH3** are shown in Figs. 12 and 13, respectively.

For the **INH1** cocrystal, N–H···O hydrogen bonding intermolecular interactions appear as two sharp small spikes in the 2D fingerprint plots, which have the most significant contribution to the total Hirshfeld surfaces of **INH1**, comprised of 34.1%, while O–H···N hydrogen bonding interactions appear as a single, sharp small spike in the 2D fingerprint plots and comprises only 1.3% of the total Hirshfeld surfaces. These hydrogen bonding interactions represent the closest contacts in the cocrystal. The H···H interactions reflected in the middle of scattered points in the 2D fingerprint plot comprises 33.3% of the total Hirshfeld surfaces. The C–H···π interactions also have a relatively significant contribution to the total Hirshfeld surfaces of the **INH1** cocrystal, comprised of 16.3%, as was indicated by the "wings" in the upper left and lower right parts of the 2D fingerprint plot. Apart from those above, the presence of π···π (C···C), lone-pair···π (N–C, O–C), and lone-pair···lone-pair (O–O, O–N, and N–N) interactions was observed, which was summarized in Table 6.

The Hirshfeld surface analysis for INH in the **INH2** cocrystal was different from that for **INH1** and **INH3**. The H–H interactions have the most significant contribution to the total Hirshfeld surfaces of the **INH3** cocrystal, which comprise 47.3% instead of the N–H···O hydrogen bonding interactions which comprise 25.4%. The O–H···N hydrogen bonding interaction was slightly larger than those in **INH1** and **INH3** (15.7%). The C–H···π interactions contribute 6.0% to the total Hirshfeld surfaces and lie in between the same item of **INH1** and **INH3**.

The Hirshfeld surface analysis for INH in the **INH3** cocrystal was similar to that for **INH1**. The N–H···O hydrogen bonding interactions still have the most significant contribution to the total Hirshfeld surfaces of the **INH3** cocrystal (32.9%), slightly smaller than that in **INH1** and a longer contact, then followed by H···H interactions (30.2%) and O–H···N hydrogen bonding interactions (6.6%), where the former is smaller than that in **INH1**, while the latter is larger. The C–H···π interactions contribute 14.5% to the total Hirshfeld surfaces and are also characterized as "wings" in the upper left and lower right parts of the 2D fingerprint plots. The other contacts were also summarized in Table 6.

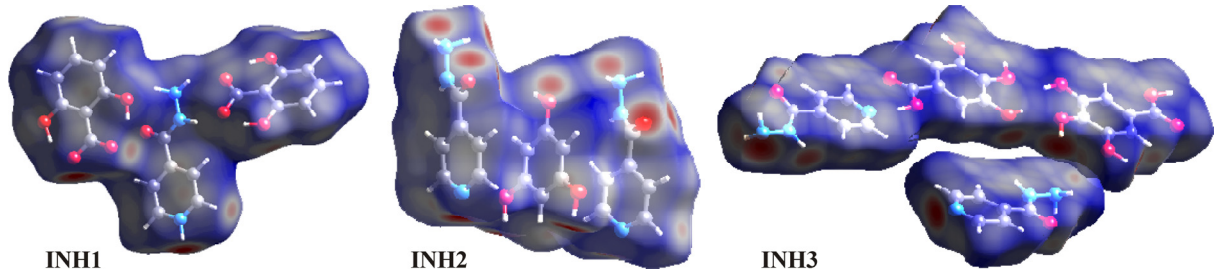

Fig. 12. Hirshfeld 3D d_{norm} surfaces in **INH1**, **INH2** and **INH3**.

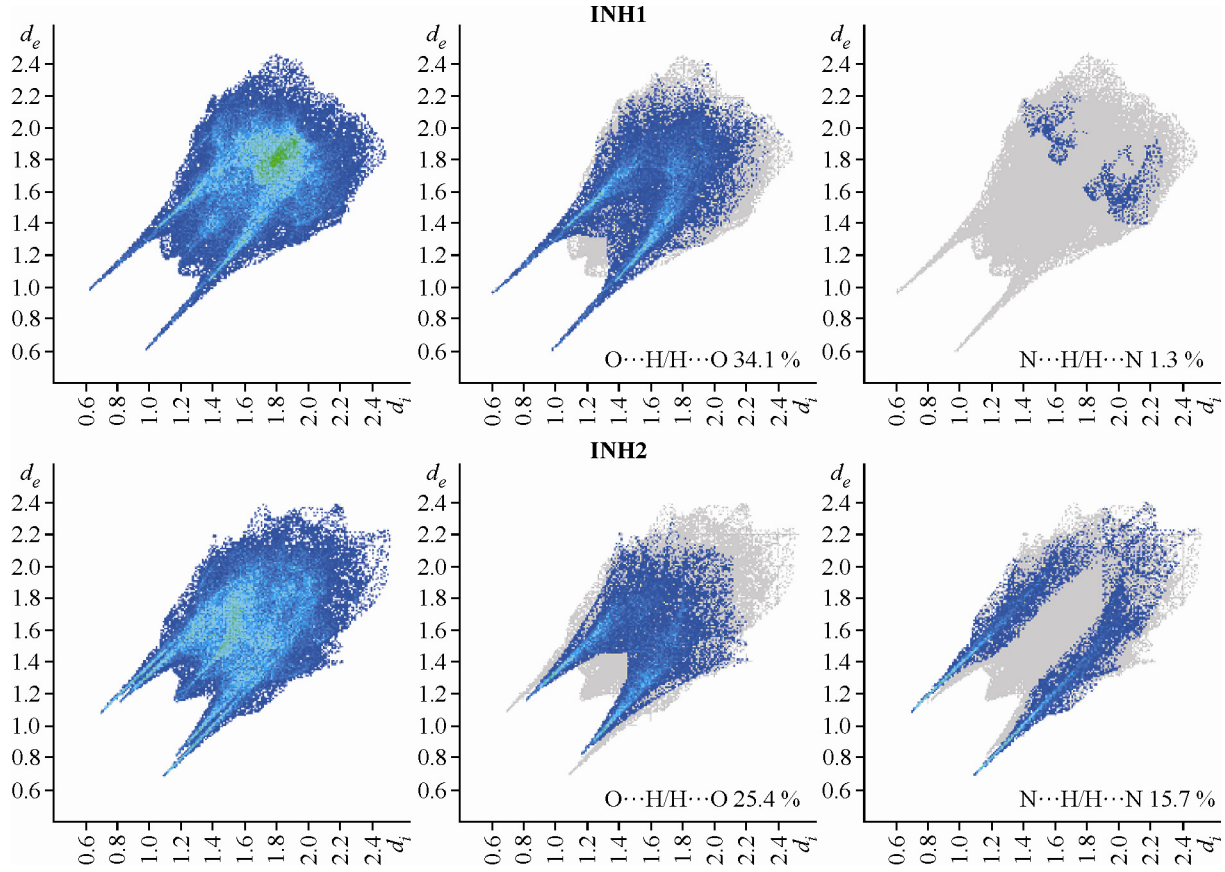

Fig. 13. 2D fingerprint plots: All contacts (left) and resolved into O···H/H···O and N···H/H···N contacts for **INH1**, **INH2** and **INH3** showing percentage of contacts contributed to the total Hirshfeld surface area of the molecules.

TABLE 6. Calculated Total Energy, HUMO, LUMO Energies, Dipole Moment, and Chemical Hardness (η) of Title Compounds Using B3LYP/6-31G(*d*,*p*) Level

Property	**INH1**	**INH2**	**INH3**
E_{tot}, Hatress	–1614.909	–1402.5786	–2237.1257
E_{HOMO}, eV	3.2623	2.2561	1.8124
E_{LUMO}, eV	4.9593	5.4530	5.8194
Dipole moment, D	10.2455	8.4669	2.8351
η, eV	0.8480	1.5982	2.003

CONCLUSIONS

Three new solid phases of the antituberculosis drug isoniazid were synthesized by the solution crystallization method. The crystalline forms were fully analyzed by the single crystal XRD analysis. The crystal forms are stabilized by various non-covalent interactions such as N^+–H···O^-, N–HO, O–H···O hydrogen bonding interactions and π–π stacking. The detailed structural investigation revealed that INH formed the 1:2 molecular complex with γRA (**INH1**), the 2:1 molecular adduct with PG (**INH2**), and the 1:1 complex with GA (**INH3**). We calculated the band structure and the total and projected DOS of the title compounds using the DFT technique in the LDA approximation. DOS calculations show that in three compounds the upper part of the valence band, the N2*p*, O2*p*, and C2*p* orbitals play a main role in TDOS, whereas the lower part of the conduction band is dominated by C2*p* and N2*p* and also a very small contribution from H1s and O2*p* states. From

the band structure calculations, we have observed that the three cocrystals had a low band gap energy in the range 1.0-2.5 eV. Therefore, at the appropriate excitation energy the electron transition is easy in C2*p*, N2*p*, and O2*p* states, which indicates that the three compounds may have some distinct optical properties. The Hirshfeld surface analysis and the 2D finger print analysis show that the N–H···O hydrogen bonding interactions for INH in all three molecular complexes follow the order **INH1** > **INH3** > **INH2**, while the O–H···N interactions follow the order **INH2** > **INH3** > **INH1**. The H···H and C–H···π interactions have a relatively significant contribution to the total Hirshfeld surfaces.

The author thanks DST-SERB (EMR/2016/001226), India for the support. CCDC reference numbers 906097 (**INH1**), 912495 (**INH2**) and 917543 (**INH3**).

REFERENCES

1. G. R. Desiraju. *Acc. Chem. Res*., **2002**, *35*, 565.
2. B. Moulton and M. J. Zaworotko. *Chem. Rev*., **2001**, *101*, 1629-1658.
3. L. MacGillivray. *CrystEngComm*., **2004**, *6*, 77/78.
4. C. B. Aakeroy and D. J. Salmon. *CrystEngComm*, **2005**, *7*, 439-448.
5. M. C. Etter. *Acc. Chem. Res*., **1990**, *23*, 120-126.
6. P. Sanphui, G. Bolla, and A. Nangia. *Cryst. Growth Des*., **2012**, *12*(*4*), 2023-2036.
7. F. T. Martins, R. Bonfilio, M. B. D. Araujo, and J. Ellena. *J. Pharm. Sci*., **2012**, *101*, 2143-2154.
8. A. T. M. Serajuddin. *Adv. Drug Delivery Rev*., **2007**, *59*, 603-616.
9. A. Lemmerer. *CrystEngComm*, **2012**, *14*, 2465-2478.
10. Ö. Almarsson and M. J. Zaworotko. *Chem. Commun*., **2004**, *0*, 1889-1896.
11. N. Blagden, M. de Matas, P. T. Gavan, and P. York. *Adv. Drug Delivery Rev*., **2007**, *59*, 617-630.
12. P. H. Stahl and C. G. Wermuth. Ed. Verlag Helvetica Chimica Acta, Zūrich, **2002**.
13. R. C. Rowe, P. J. Sheskey, and S. C. Owen. Ed. APhA Publications, 5th edn, **2005**.
14. USP DI®, vol. I, 15th ed. 1627, **1995**.
15. A. Lemmerer, J. Bernstein, and V. Kahlenberg. *CrystEngComm*, **2010**, *12*, 2856-2864.
16. P. Grobely, A. Mukherjee, and G. R. Desiraju. *CrystEngComm*, **2011**, *13*, 4358-4364.
17. N. Ravikumar, G. Gopikrishna, and K. Anand Solomon. *J. Mol. Struct*., **2013**, *1033*, 272-279.
18. A. Lemmerer, J. Bernstein, and V. Kahlenberg. *J. Chem. Crystallogr*., **2011**, *41*, 991-997.
19. S. Cherukuveda and A. Nangia. *CrystEngComm*, **2012**, *14*, 2579-2588.
20. J. G. da Silva Filho, V. N. Freire, E. W. S. Caetano, L. O. Ladeira, U. L. Fulco, and E. L. Albuquerque. *Chem. Phys. Lett*., **2013**, *587*, 20-24.
21. X.-G. Meng, Y.-L. Xiao, H. Zhang, and C.-S. Zhou. *Acta. Crystallogr.*, *Sect. C*, **2008**, *64*, o261-o263.
22. I. Sarcevica, L. Orola, M. V. Veidis, A. Podjava, and S. Belyakov. *Cryst. Growth Des*., **2013**, *13*, 1082-1090.
23. N. Saikia, S. K. Pati, and R. C. Deka. *Appl. Nanosci*., **2012**, *2*, 389-400.
24. B. Barbielini and A. Shukla. *Phys. Rev. B*, **2002**, *66*, 235101.
25. Bruker APEX2, SAINT, SADABS. Bruker AXS Inc., Madison, Wisconsin, USA, **2004**.
26. A. Altomare, G. Cascarano, C. Giacovazzo, and A. Guagliardi. *J. Appl. Crystallogr*., **1993**, *26*, 343-350.
27. G. M. Sheldrick. *Acta Crystallogr*., **2008**, *A64*, 112-122.
28. M. Segall, P. Linda, M. Probert, C. Pickard, C. Hasnip, S. Clark, and M. Payne. Materials Studio CASTEP, version 2.2. AccelrysSan Diego, CA, **2002**.
29. M. J. Frisch, G. W. Trucks, H. B. Schlegel, G. E. Scuseria, M. A. Robb, J. R. Cheeseman, et al. Gaussian 09, Revision A.02. Gaussian, Inc., Wallingford CT, **2009**.
30. S. K. Wolff, D. J. Grimwood, J. J. McKinnon, D. Jayatilaka, and M. A. Spackman. Crystal Explorer, version 1.5, University of Western Australia: Perth, Australia, **2007**.

31. F. P. A. Fabbiani, L. T. Byrne, J. J. McKinnon, and M. A. Spackman. *CrystEngComm*, **2007**, *9*, 728-731.
32. A. Parkin, G. Barr, W. Dong, C. J. Gilmore, D. Jayatilaka, J. J. McKinnon, M. A. Spackman, and C. C. Wilson. *CrystEngComm*, **2007**, *9*, 648-652.
33. M. A. Elbagerma, H. G. M. Edwards, T. Munshi, M. D. Hargreaves, P. Matousek, and I. J. Scowen. *Cryst. Growth Des*., **2010**, *10*, 2360-2371.
34. S. L. Childs, G. P. Stahly, and A. Park. *Mol. Pharmaceutics*, **2007**, *4*, 323-338.
35. R. M. Silverstein and F. X. Webster. Spectrometric identification of organic compounds 6th edn. Wiley, New York, **1998**.
36. E. Spinner. *J. Chem. Soc*., **1962**, *10*, 3119.
37. P. Bassignana, C. Cogrossi, and M. Gaudino. *Spectrochim*. *Acta*, **1963**, *19*, 1885-1897.
38. T. Thakuria and A. Nangia. *CrystEngComm*, **2011**, *13*, 1759-1764.
39. J. F. Remenar, M. L. Peterson, P. W. Stephens, Z. Zhang, Y. Zimenkov, and M. B. Hickey. *Mol. Pharmaceutics*, **2007**, *4*, 386-400.
40. T. A. Koopmans. *Atoms Physica*, **1934**, *1*, 104-113.
41. P. Sjoberg and P. Politzer. *J. Phys. Chem*., **1990**, *94*, 3959-3961.
42. J. J. McKinnon, D. Jayatilaka, and M. A. Spackman. *Chem. Commun*., **2007**, *12*, 3814-3816.
43. M. A. Spackman and D. Jayatilaka. *CrystEngComm*, **2009**, *11*, 19-32.
44. M. J. Turner, J. J. McKinnon, D. Jayatilaka, and M. A. Spackman. *CrystEngComm*, **2011**, *13*, 1804-1813.
45. M. A. Spackman, J. J. McKinnon, and D. Jayatilaka. *CrystEngComm*, **2008**, *10*, 377-388.